Improving Land Cover Change Detection and Classification With BRDF Correction and Spatial Feature Extraction Using Landsat Time Series: A Case of Urbanization in Tianjin, China

Yuwei Guan, Yanru Zhou, Binbin He, Xiangzhuo Liu, Hongguo Zhang, and Shilei Feng

***Abstract*—As one of the important coastal cities in China, Tianjin has been urbanized dramatically over the past 40 years, and the urbanization rate has been up to 83.15% by 2018. In this study, we used the continuous change detection and classification algorithm to comprehensively understand the urban expansion processes in Tianjin based on the Landsat time series from 1985 to 2018 with 30-m resolution. Specially, we applied the c-factor approach with the Ross Thick-LiSparse-R model to correct the bidirectional reflectance distribution function (BRDF) effect for each Landsat image and calculated a spatial line density feature for improving the change detection and the classification. Based on the study in Tianjin, we found that BRDF correction can substantially improve the change detection (9.00% higher overall accuracy) and classification (1.08% higher overall accuracy); and the line density is also beneficial to classification (0.48% higher overall accuracy), especially for impervious surface (1.70% less commission errors and 1.49 % less omission errors). By analyzing the imperious surface change processes, we observed that Tianjin has undergone rapid urban expansion in the past decades, and the urban area was mainly transformed from cropland around the central area before 2005 and later from the coast.**

***Index Terms*—Bidirectional reflectance distribution function (BRDF), continuous change detection and classification (CCDC), Landsat time series (LTS), line density, Tianjin, urbanization.**

I. Introduction

URBANIZATION has been an important social and economic phenomenon taking place at an unprecedented scale and rate all over the world [1]. As an important port and transportation hub in China, Tianjin has experienced rapid urban expansion since the Chinese reform and opening in 1978. Understanding the urban expansion processes of Tianjin is vital for guiding the future urban management and sustainable development planning [2].

To understand the dynamics of urban expansion processes, long-term land change and land cover data are required [3], and the Landsat time series (LTS) with 30-m spatial resolution and 8-d temporal resolution has become one of most valuable datasets for this task [3], [4]. Currently, lots of LTS-based algorithms have been proposed for change detection especially since the free and open policy was implemented in 2008 [5], [6]. Kennedy *et al*. [7] proposed Landsat-based detection of trends in disturbance and recovery (LandTrendr) for identifying spectral trajectories of surface changes by yearly LTS. It is based on temporal segmentation and it can capture gradual change (e.g., regrowth) and abrupt change (e.g., deforestation). However, the yearly spectral deviation heavily depends on the observations acquired in neighboring years, and thus it is hard to identify the changes in the first and last year. Huang *et al*. [8] developed a vegetation change tracker based on the spectral-temporal characteristics of land cover and forest change processes. Hamunyela *et al*. [9] used spatial contexts to reduce seasonal variations in LTS data, which can detect deforestation events well. Both of them were designed especially for forest disturbances, being less applicable for dynamics in other kinds of land cover (e.g., urban area) [10]. The breaks for additive season and trend algorithm was designed for detecting change based on MODIS time series, by decomposing the entire time series into trend, season, and noise components [11], [12]. Recently, it also shows potential availability of monitoring forest disturbances [9, 13], agriculture cultivation [14], and wetland dynamic [15] from LTS; but few of them focused on impervious surface. The continuous change detection and classification (CCDC) algorithm used all spectral bands to detect various kinds of land cover change continuously [16], [17]. It has been implemented into the USGS land change monitoring, assessment, and projection (LCMAP) program for generating land cover and land change products for the United States [18]–[20] and also widely used in many applications, such as urban expansion [19], [21], [22], hydrology dynamic [23], and forest disturbance [24].

Manuscript received February 5, 2020; revised April 30, 2020, June 10, 2020, and June 22, 2020; accepted June 22, 2020. Date of publication July 7, 2020; date of current version July 30, 2020. This work was supported in part by the Fundamental Research Fund for the National Key Research and Development (R&D) Program of China under Contract 2018YFD0200301 and in part by the National Natural Science Foundation of China under Contract 41671361. *(Corresponding author: Binbin He.)*

Yuwei Guan, Yanru Zhou, Xiangzhuo Liu, Hongguo Zhang, and Shilei Feng are with the School of Resources and Environment, University of Electronic Science and Technology of China, Chengdu 611731, China (e-mail: guanyuwei@uestc.edu.cn; 857702622@qq.com; 1183436081@qq.com; 369910038@qq.com; 2812155690@qq.com).

Binbin He is with the School of Resources and Environment, University of Electronic Science and Technology of China, Chengdu 611731, China, and also with the Center for Information Geoscience, University of Electronic Science and Technology of China, Chengdu 611731, China (e-mail: binbinhe@uestc.edu.cn).

Digital Object Identifier 10.1109/JSTARS.2020.3007562

Although LTS has been widely used to detect land cover changes, the LTS temporal consistency has received less attention. For data consistency, we can define that "simultaneous collection images should have exactly the same value" [25]. One of the crucial issues is the effect of solar-surface-sensor geometry, often described as bidirectional reflectance distribution function (BRDF), especially when the images are acquired from adjacent satellite orbit swaths [26]. Note that the orbit of drift Landsat satellite would also influence the BRDF [26]. In this case, the BRDF effect is particularly significant since for same pixel the sensor view angles can vary from $-7.5°$ to $7.5°$ and the solar angles will also be different at different acquisition dates [27]. Although, BRDF correction can significantly improve the temporal consistency of LTS [25], its effect on change detection accuracy still needs to be quantitatively answered.

Land cover classification has attracted attention for many years. The traditional approach only requires single-date image and calculates spectral and spatial features to classify different land cover types. For example, Guindon *et al*. [28] classified different kinds of land cover using spectral bands, and also used a spatial rule to optimize the final map. Zhang *et al*. [29] proposed a spectral-spatial approach to extract urban area from Landsat images by combining multivariate variogram textures and spectral information. Recently, extra temporal features can be derived from time series of satellite observations to improve the classification accuracy greatly [30]–[32]. Jia *et al*. [33] used single-date Landsat eight data to classify different land cover types, but extra integrated temporal features downscaled from time series of MODIS normalized difference vegetation index to improve the classification accuracy. In addition to change detection, the CCDC algorithm can classify land cover using the information in spectral and temporal dimensions [16]. Although, these time-series-based classification approaches can take advantage of spectral and temporal features, few of them considered the spatial information to improve classification. Therefore, it is expected that the fusion of spatial, spectral, and temporal dimensions can generate better classification results.

In this study, we selected the widely used CCDC algorithm [16] as the core to detect land cover change and classify land cover types, but mainly focused on assessing whether BRDF correction can improve the change detection and classification of land cover, integrating a spatial line-density feature to improve the classification of land cover especially for impervious surface, and applying it to analyze the temporal-spatial change of impervious surface (it is the most intuitive indicator of urbanization [34]) and the land cover conversion in Tianjin, China over the past decades.

II. Study Area and Data

A. Study Area

The study area is located in Tianjin, China, of which the area is about 12,000 km^2 (Fig. 1). As the center of the Bohai economic circle, Tianjin has been known as the "third growth pole of the Chinese economy" [35]. This area includes kinds of land cover such as cropland, forest, grassland, water, impervious, and bareland. At the same time, it has experienced dramatic urbanization over the past 40 years. Therefore, Tianjin is a good study area to test the approach of land cover change and classification, and its historical change process also needs to be well understood.

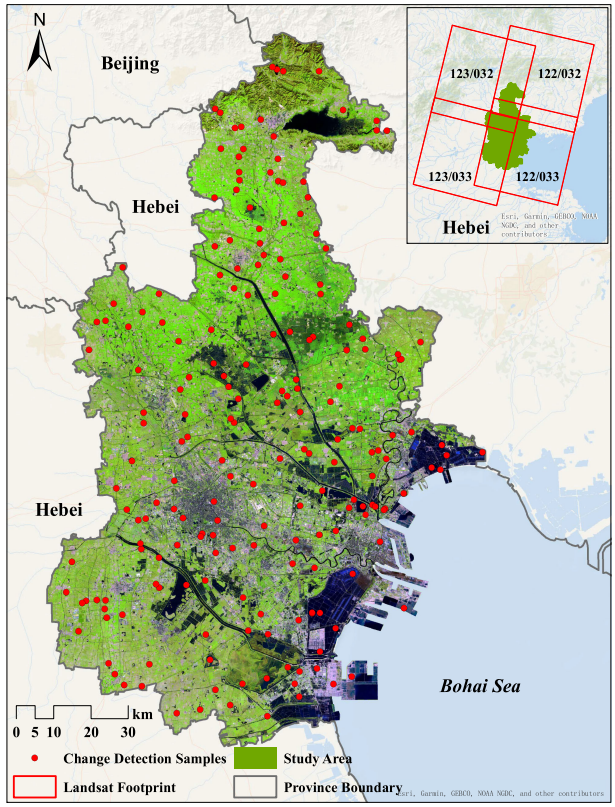

Fig. 1. Study area (Tianjin, China). The background is CCDC synthesized Landsat image on July 1, 2018 (composed by SWIR1, NIR, and Red Bands).

TABLE I
Landsat Data Used in This Study

Path/Row	Number of Landsat 4-5/7/8
122/032	368/299/96
122/033	363/285/95
123/032	339/285/85
123/033	323/247/80

B. Data

1) Landsat Data: Four Landsat Collection 1 scenes, provided in the worldwide reference system two path/row, were used for covering the entire Tianjin (Fig. 1). In each Landsat scene, we downloaded all available images with cloud cover less than 80% from 1985 to 2018 (Table I), which include surface reflectance, brightness temperature (BT), solar/sensor angles, and quality assurance (QA) band. The QA band can provide the mask of clouds and cloud shadows generated by the CFmask (C version of Fmask) algorithm [36]. Note that the overlapped areas by adjacent Landsat images also provide good locations to study the effect of BRDF on change detection and classification.

2) Land Cover Change Reference: We randomly selected 200 points over the study area to generate the land cover change reference data. In each point, we manually interpret when the change occurred based on the corresponding LTS, with aid of

TABLE II
LAND COVER TYPES

Land Cover	Number of samples	Description
Cropland	2187	Lands with intensive human activity (excluding pasture grass). (55.64% in GLC product)
Forest	24	Areas with tree cover over 15% and tree height over 3 meters. (3.83% in GLC product)
Grassland	39	Herbal plant coverage greater than 15%.(2.04% in GLC product)
Water	1557	Natural and artificial water bodies. (11.17% in GLC product)
Impervious	1069	Artificial surface and related areas. (25.30% in GLC product)
Bareland	83	Non-artificial surface with little or no vegetation. (2.02% in GLC product)

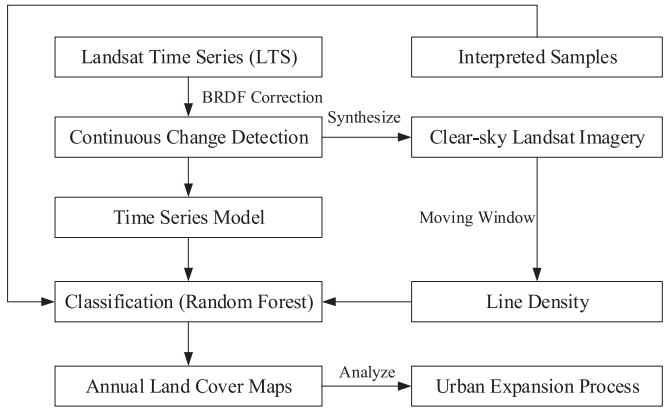

Fig. 2. Flowchart of the approach in this study. The components of CCDC are from the CCDC algorithm.

Google Earth historical high resolution (HHR) images. If there are multiple changes over one location, we only consider the last (or cumulative) change to validate since we do not want the pixels with multiple changes to bias the accuracy. This finally gave us 98 changed pixels and 102 stable pixels (no change within the entire LTS) (Fig. 1), which will be used to validate the change detection results.

3) Land Cover Reference: Since the land cover reference data collected in any analysis period (1985–2018) can be used for training classification model of the CCDC algorithm [16], we selected a total of 6 000 sample points over the whole study region randomly from the finer resolution observation and monitoring of global land cover (FROM-GLC) map in 2017 [37]. The FROM-GLC is the first 30-m resolution global land cover maps produced using Landsat thematic mapper and enhanced thematic mapper plus (ETM+) data [38]. To ensure the accuracy of our samples, for each sample we further carefully interpreted the corresponding Google Earth HHR and Landsat image to correct the wrong land cover types. At the same time, we excluded the samples that we cannot make the confident interpretation. Finally, a total of 4 959 land cover samples were collected for training and validation (Table II).

III. METHODS

We use the CCDC algorithm [16] as the basis for land cover change detection and classification due to its relatively high accuracy and easy-to-use. Built on the CCDC algorithm, in this study, we will correct the BRDF effect for each Landsat image to build a more consistent LTS and expect that this can improve both change detection and classification. At the same time, a spatial feature (i.e., line density) will be computed for improving the classification. Finally, the urban expansion in Tianjin will be quantitatively described based on the annual land cover products for the past decades. Fig. 2 illustrates the flowchart of this study.

A. CCDC Algorithm

The CCDC algorithm is based on the LTS without (or at least with few) noises such as clouds and cloud shadows, and requires the surface reflectance of blue, green, red, NIR, and two SWIR bands and the BT of thermal band as the inputs [16], [17]. The clouds and cloud shadows can be screened out by CFmask (derived from QA band) [36] and multiTemporal mask algorithm [39], which are integrated in CCDC package. For each individual pixel, it can continuously detect various land cover changes once new Landsat images are collected. CCDC can predict observations for each band based on three sets of Fourier models (e.g., simple with ($k = 1$), and advanced ($k = 2$), and full ($k = 3$)) (1) [17]. The simple model requires at least 12 clear-sky Landsat observations, whereas 18∼24 clear-sky observations will generate the advanced model. If more than 24 clear-sky observations, the full model will be triggered. A more complex time series model would better model the intraannual variations. By comparing the model predictions and the actual satellite observations six times consecutively, the CCDC algorithm can identify land cover changes. If a change is detected, two time series segments will be generated before and after the change; or, only one time series segment will be generated for the stable pixel (no change).

In each time series segment, the coefficients and root mean square errors (RMSE) of the corresponding model for each band (they can provide spectral and temporal information at the same time) will be inputted into random forest (RF) model to classify different kinds of land cover types [16]. Note the overall value (a_0) will be adjusted by adding the original value (a_0) and the slope (c_1) multiplied by the middle time of the time series segment [16]. Besides of those coefficients, we extra computed a spatial feature (line density) to improve the classification performance (see Section III-C for details).

$$\hat{\rho}_{i,t} = a_{0,i} + c_{1,i}t + \sum_{k=1}^{3}\left(a_{k,i}\cos\frac{2k\pi t}{T} + b_{k,i}\sin\frac{2k\pi t}{T}\right) \quad (1)$$

where t is the Julian date; i is the ith Landsat band ($i = 1, 2, 3, 4, 5,$ and 7); k is the temporal frequanct of Fourier component ($k = 1, 2,$ and 3); T is the number of days per year (365.25); $a_{0,i}, c_{1,i}$are the overall (intercept) and interal-annual change (slope) coefficients for the ith Landsat band; $a_{k,i}$ and $b_{k,i}$ are the intraannual change coefficients for the ith Landsat band; $\hat{\rho}_{i,t}$

is the predicted surface reflectance for the *i*th Landsat band at the Julian date *t*.

B. BRDF Correction for Improving Change Detection

A temporally consistent LTS is often expected for change detection, but the images would be significantly affected by the BRDF effects especially when the images are from adjacent Landsat orbit swaths (overlapped area) [25]. To eliminate the BRDF effects in LTS, we use the c-factor method with the Ross Thick-LiSparse-R model [25], [27], [40] (2) for each Landsat image and expect this can be beneficial to improve accuracy of change detection. Note that the normalized solar zenith angle (Ω') is determined by the central latitude of Landsat image (3) [41].

$$\rho' = \rho \cdot \frac{f_{\text{iso}} + f_{\text{vol}} \cdot K_{\text{vol}}(\Omega', 0^\circ, 0^\circ) + f_{\text{geo}} \cdot K_{\text{geo}}(\Omega', 0^\circ, 0^\circ)}{f_{\text{iso}} + f_{\text{vol}} \cdot K_{\text{vol}}(\Omega, \alpha, \beta) + f_{\text{geo}} \cdot K_{\text{geo}}(\Omega, \alpha, \beta)} \tag{2}$$

where α is the view zenith angle; β is view-sun relative azimuth angle; Ω is the solar zenith angle; Ω' is the normalized solar zenith angle [determined by (3)]; ρ is the original reflectance;ρ' is the BRDF-normalized reflectance (at nadir); f_{iso},f_{vol}, and f_{geo} are the BRDF model parameters [40]; $K_{vol}(\Omega, \alpha, \beta)$ and $K_{geo}(\Omega, \alpha, \beta)$ are the Ross Thick kernel and the LiSparse-R kernel, respectively [42].

$$\begin{aligned}\Omega' = {} & 31.0076 - 0.1272 \times \mu + 0.01187 \times \mu^2 + 2.4 \times 10^{-5} \\ & \times \mu^3 - 9.48 \times 10^{-7} \times \mu^4 - 1.95 \times 10^{9} \times \mu^5 \\ & + 6.15 \times 10^{-11} \times \mu^6 \end{aligned} \tag{3}$$

where μ is the central latitude of Landsat scene.

C. Line Density for Improving Classification

We generated annual land cover products based on the CCDC algorithm, but extra integrated a line-density feature to improve them. The calculation of the line density is based on a clear-sky Landsat image of each year, and the basic idea is that lines can be extracted using a combination of an unsupervised cluster model (e.g., K-Means) and a morphological approach (e.g., expansion and corrosion) and then the line density will be computed using a moving window.

As it is difficult to obtain a perfect clear-sky Landsat image, we used the CCDC algorithm to synthesize a Landsat image on July 1 (middle day) for each year [17]. July 1 was selected mainly because the spectral aliasing problem can be significantly reduced in summer [43]. The synthetic Landsat image will be segmented into lots of objects using the K-Means clustering algorithm [44]. In the K-Means, the key parameter is the number of clusters and we set this six by following the number of land cover categories in the reference data [45]. For each object, we extracted the boundaries using a simple morphological edge detector with a size of 3 pixels × 3 pixels such as the expansion-corrosion residue operator [46], [47], and only remained the straight lines by a spatial convolution with four direction templates (Fig. 3). The spatial convolution will filter each pixel in the boundary image using each of the template and retain the maximum response, which can highlight the straight line features in urban

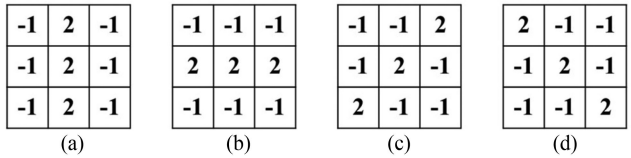

Fig. 3. Four line-enhancement kernels which respond maximally to horizontal, vertical, and oblique (+45° and −45°) lines.

Fig. 4. Line-density image in 2017.

(e.g., roads) [48]. Finally, a moving window of 7 pixels × 7 pixels is used to calculate the line density, which is the area ratio of the remaining straight lines and the entire window [49]. The window size was determined by visual assessment and a size of 7 can provide a good layer to highlight urban area (Fig. 4).

We generated the annual land cover map on July 1 (middle day) as a representative of the annual status by following LCMAP program [20]. For each year, we extracted the coefficients and RMSE of the time-series segments in CCDC across July 1, and combined them with the line density (spatial information) together to produce annual land cover maps.

D. Urban Expansion Analysis

We applied the CCDC algorithm with line density to generate the annual land cover products (on July 1, full sample training) from 1985 to 2018 based on BRDF-corrected LTS since we found that both BRDF correction and the line density

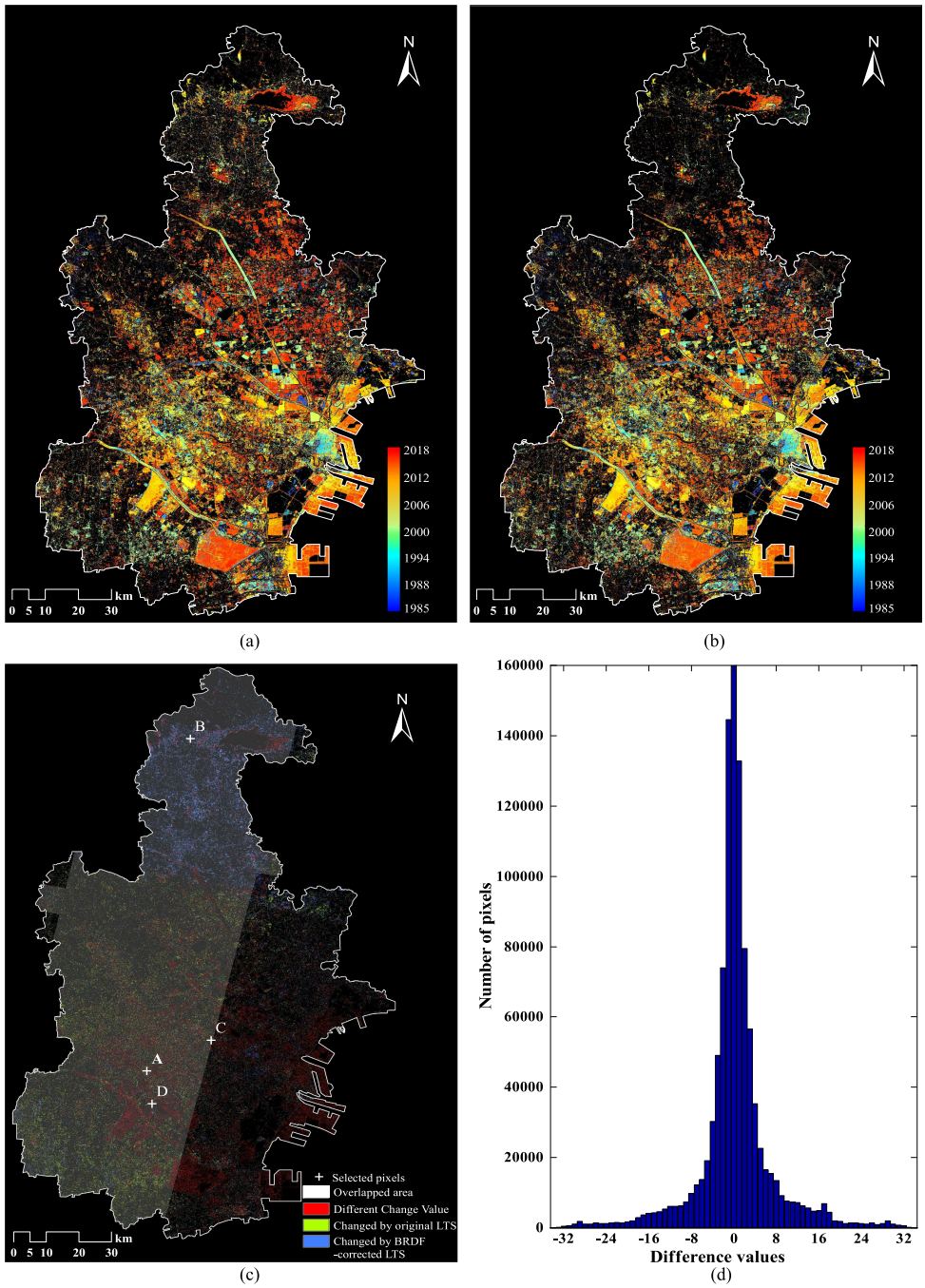

Fig. 5. Accumulated change map based on original LTS versus BRDF-corrected LTS. (a) Accumulated change map based on the original LTS. (b) Accumulated change map based on the BRDF-corrected LTS. (c) Different between (a) and (b). Overlap area is from the Landsat footprints (65.2% of the entire study area are located at the overlapped areas). (d) Histogram of difference for change values (the year of the last detected change) (1985–2018).

can improve the results (see Section IV for details). Although, the annual products will not present the near-real time changes detected by CCDC, it would not seriously affect the analysis of the urbanization at such a long period. In order to comprehend the urbanization processes, in this study, we mainly consider the impervious surface distribution and changes. To quantitatively describe the mutual transformation relationship between the impervious surface and other land covers in the process, we will calculate the annual land cover transfer matrix based on the land cover products.

IV. Results and Discussions

A. Improvement of BRDF Correction on Change Detection

We used the CCDC algorithm to detect change but also focused on the effects of BRDF correction on LTS. Since there are only limited number of changes in each individual year, the annual change map can be accumulated into one (hereafter "accumulated change map"), so that the changes can be observed in a continuous mode, and the accumulated map does show out the last changes detected by CCDC. Fig. 5 compares the

TABLE III
COMPARISON OF CHANGE DETECTION ACCURACY BEFORE AND AFTER BRDF CORRECTION

		Visual		
		Changed Pixels	Stable Pixels	User's (%)
Original LTS	Changed Pixels	**80**	13	86.02
	Stable Pixels	18	**89**	83.18
	Producer's (%)	81.63	87.25	**Overall 84.50**
BRDF-corrected LTS	Changed Pixels	**90**	5	94.74
	Stable Pixels	8	**97**	92.38
	Producer's (%)	91.84	95.10	**Overall 93.50**

accumulated change detection result from the original LTS and that from the BRDF-corrected LTS. Although, the two results are generally similar [Fig. 5(a) versus (b)], most of the differences (green and blue colors) can be observed from the overlap areas between different Landsat scenes [Fig. 5(c)]. Fig. 5(d) shows the histogram of the difference for change years from the accumulated change maps based on the original LTS and the BRDF-corrected LTS. Most of the differences in the last change value are less than five years (partially due to that the last or accumulated change were focused), although there are some large differences. Against the selected sample pixels located in the overlap areas with large differences, the visual assessment indicates that the BRDF-corrected LTS can result in better detection of land cover changes (Fig. 6). Fig. 6(a) shows that cropland was changed to develop. The change is properly detected using the BRDF-corrected LTS, but omitted from the original LTS. Fig. 6(b) shows that the BRDF-corrected LTS generated a better result over the location where the developed area has no change. Fig. 6(c) shows a pixel where a change process occurred in the past years, but the results using the original LTS are incorrect. Fig. 6(d) shows there is a change from low-intensity to high-intensity developed area that can be correctly identified by CCDC if we use the BRDF corrected LTS. Table III shows the confusion matrix for the results using original LTS and using BRDF-corrected LTS. Compared to the original LTS, the BRDF-corrected LTS can improve the change detection accuracy significantly (84.50% versus 93.50%). Additionally, both producer's and the user's accuracy for change and stable samples are higher, which mean BRDF correction can reduce the omission and commission errors at the same time. This is mainly because that BRDF correction can result in an LTS with better temporal consistency, and further improve the estimation of the time series model in CCDC. We observed BRDF correction cannot vary the reflectance too much for each individual observation, but BRDF correction would make the entire LTS more consistent [25]. This means that the BRDF-corrected LTS can better predict CCDC time series model, with a smaller RMSE value (Fig. 6). CCDC detects change by comparing model predictions and satellite observations; but the change detection threshold is adjusted based on the RMSE. A smaller RMSE would reasonably provide with a smaller threshold to detect changes [16]. As a result, the original LTS would omit to detect such kind of changes that only varied the reflectivity of several spectral band, but the BRDF-corrected LTS would be better [e.g., Fig. 6(a)]. In this study, we only tested the effects of BRDF correction on CCDC results in Tianjin, China, the conclusion may be different if another time series algorithm is used.

B. Improvements of BRDF Correction and Line Density on Classification

Fig. 7 visually compares the classification results with and without BDRF correction and line density. As they share a similar pattern at large scale, we only show the entire land cover map in 2017 generated by the approach using the BRDF-corrected LTS with line density (the best one). At smaller scales, compared to the results only using the original LTS, we find that the combination of BRDF correction and line density can better classify different land cover types. For example, Fig. 7(a) and (b) shows that the approach using only the original LTS misclassified cropland as forest. However, the combination of BDRF correction and line density can reduce those commission errors significantly. Fig. 7(c) and (d) shows the results in urban area where BRDF correction and line density can also improve the identification of impervious surface. Fig. 7(e) shows a cropland around water. BRDF correction and line density significantly reduce the misclassification errors of cropland as impervious surface. Fig. 7(f) shows that the original LTS led to misclassify impervious surface (e.g., roads) as water around paddy fields. Compared to the original LTS, using BRDF correction and line density reduced this kind of errors. Note since the paddy field is often flooded continually, we think classification as water is not a problem.

The accuracies are assessed using a cross validation against our 4 959 reference pixels in 2017. We randomly selected 80% of the reference data to train the RF model and utilized the remaining 20% to calculate the classification accuracy [50]. This process was repeated 20 times, and we found every time the approach with BRDF correction and line density achieved the highest overall accuracy compared to the other classification scenarios (e.g., BRDF correction only, line density only, and none of them) (Fig. 8). Table IV shows that the confusion matrix for different scenarios. Combination of BRDF correction and line density can improve 1.49% overall accuracy compared to the approach without them (88.91% versus 87.42%). If we only consider BRDF correction or line density, the overall accuracy increases with incremental magnitudes of 1.08% and 0.48%, respectively. Compared to the other land cover types, identification of impervious surface is most substantially improved, with 4.46% higher producer's accuracy and 3.04% user's accuracy.

BRDF correction is more important for improving classification compared to line density. This is mainly because BRDF correction can result in better change detection results (Table III) and indirectly affect classification of any kinds of land cover (e.g., cropland, water, and bareland); however, the line density is designed especially for the urban area. In addition, there are still lot of confusions between bareland and impervious surfaces

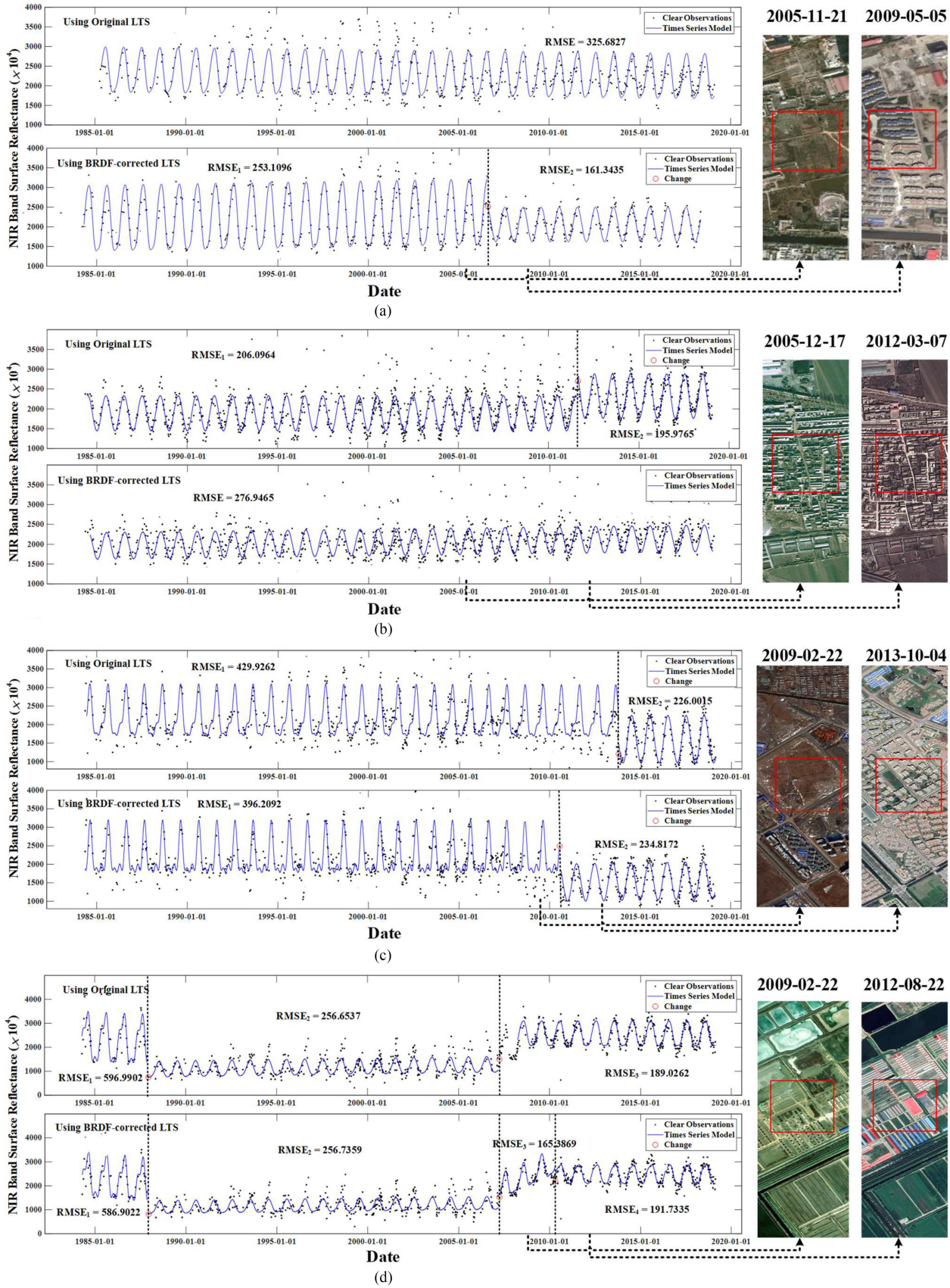

Fig. 6. Examples of change detection comparison between original LTS and BRDF-corrected LTS. (a) Cropland changes to developed at the location A in Fig. 5(c). (b) No change at the location B in Fig. 5(c). (c) One change at the location C in Fig. 5(c). (d) Change from low-intensity to high-intensity urban at the location D in Fig. 5(c). Note the right high-resolution images are from Google Earth and the red polygons indicate the Landsat observation.

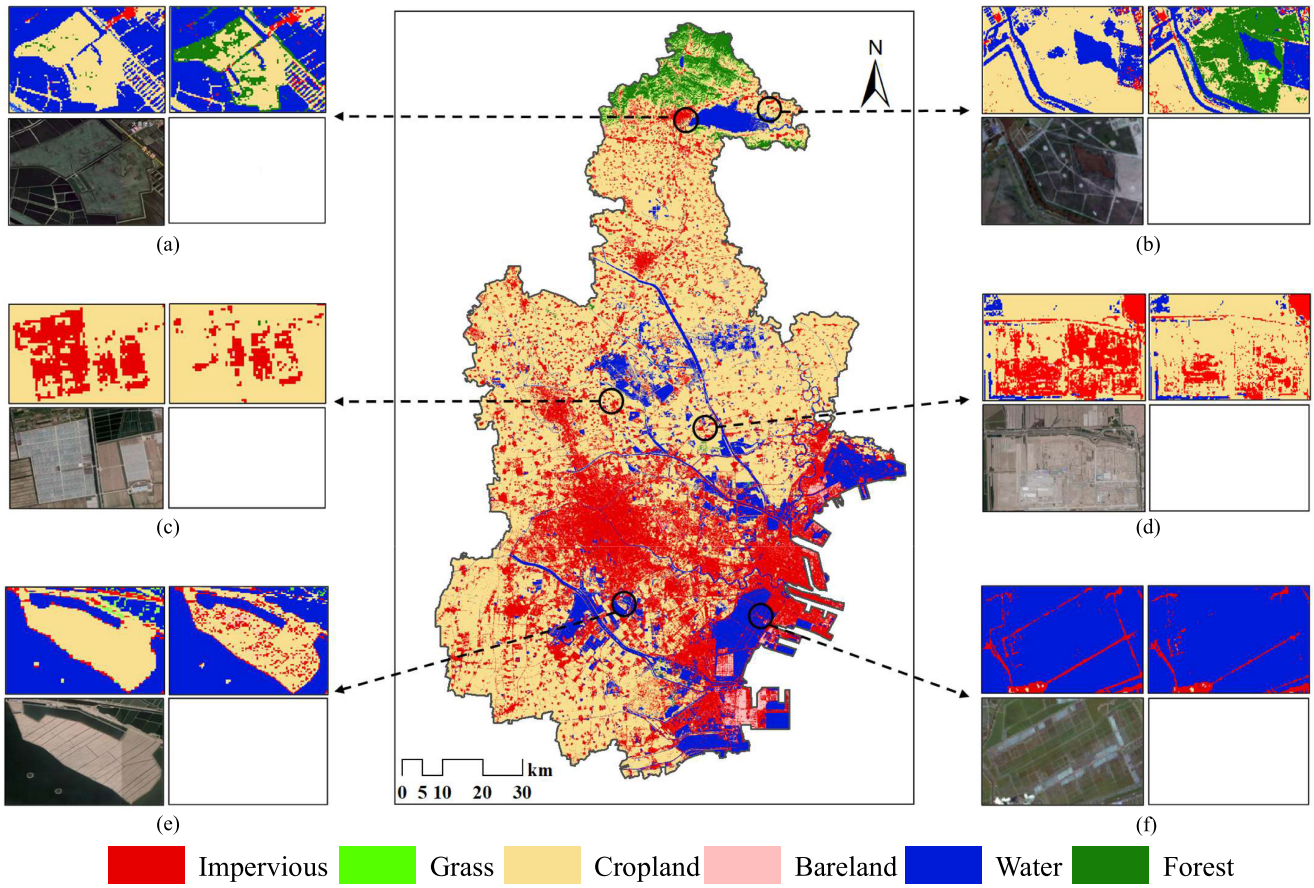

Fig. 7. Classification map in 2017. The center is the entire land cover map in 2017 generated by the CCDC algorithm using the BRDF-corrected LTS with line density. For each pop-up panel, the upper-left image shows the result using the BRDF-corrected LTS with line density. The upper-right image shows the result only using the original LTS. The lower-left image shows Google Earth HHR image in 2017.

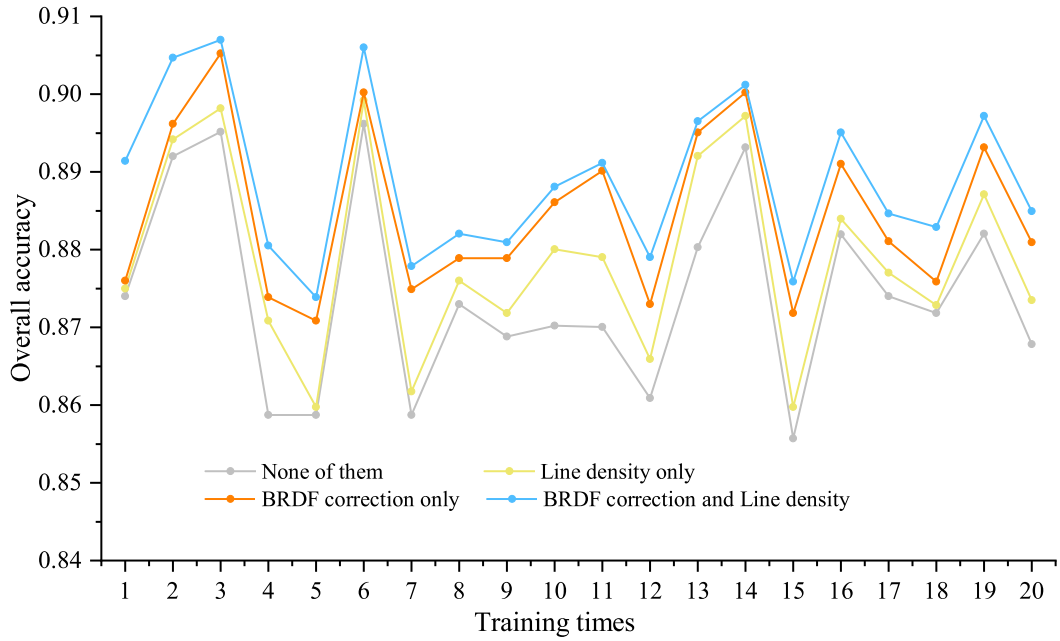

Fig. 8. Comparison of classification overall accuracy using different inputs. The cross validation with 80% for training and 20% for validating was repeated 20 times.

TABLE IV
CONFUSION MATRICES FOR ASSESSING THE ACCURACY OF CLASSIFICATION IMAGES BY DIFFERENT METHODS

		Visual						
Scenario	Land Cover	Cropland	Forest	Grass	Water	Impervious	Bareland	User's (%)
None of them	Cropland	398	4	1	9	33	0	89.44
	Forest	0	0	0	0	0	0	Na
	Grass	0	0	0	0	0	0	Na
	Water	8	1	1	305	7	0	94.72
	Impervious	39	0	4	5	161	12	72.85
	Bareland	0	0	0	0	1	3	75.00
	Producer's (%)	89.44	0.00	0.00	95.61	**79.70**	20.00	**Overall 87.42**
Line-density only	Cropland	399	4	4	8	32	0	89.26
	Forest	0	0	0	0	0	0	Na
	Grass	0	0	0	0	0	0	Na
	Water	8	1	1	306	5	0	95.33
	Impervious	38	0	1	5	164	12	**74.55**
	Bareland	0	0	0	0	1	3	75.00
	Producer's (%)	89.66	0.00	0.00	95.92	**81.19**	20.00	**Overall 87.90**
BRDF correction only	Cropland	401	5	2	8	28	0	90.32
	Forest	0	0	0	0	0	0	Na
	Grass	0	0	0	0	0	0	Na
	Water	8	0	1	305	5	0	95.61
	Impervious	36	0	3	6	167	10	**75.23**
	Bareland	0	0	0	0	2	5	71.43
	Producer's (%)	90.11	0.00	0.00	95.61	**82.67**	33.33	**Overall 88.50**
BRDF correction and Line-density	Cropland	401	5	2	8	26	0	90.72
	Forest	0	0	0	0	0	0	Na
	Grass	0	0	0	0	0	0	Na
	Water	8	0	1	305	5	0	95.61
	Impervious	36	0	3	6	170	9	**75.89**
	Bareland	0	0	0	0	1	6	85.71
	Producer's (%)	90.11	0.00	0.00	95.61	**84.16**	40.00	**Overall 88.91**

Note: Since the classification training data contains only a small number of forest and grass pixels and these two land covers are not identified well during the validation process, the user's accuracy is none (labeled as "NA").

(Table IV), although the CCDC algorithm makes full use of spectral and temporal information. This finding can also be found in the studies of Brown *et al*. [20] and Deng and Zhu [22]. Fortunately, the inclusion of spatial feature such as line density in our study can reduce the commission errors (from 40% to 33.3% of producer's accuracy and from 85.7% to 71.4% of user's accuracy for bareland).

C. Urban Expansion Processes in Tianjin

By analyzing the changes about the impervious surface, we observe that the urban expansion in Tianjin experienced two key stages (Fig. 9). The first stage is that the total area of impervious surface in Tianjin increased by 338 km^2 from 1985 to 2005, and the expansion mainly occurred around the central area (see green area in Fig. 9). The second stage is that between 2006 and 2018 the total area of new impervious surface reached 351 km^2, mainly in the coast such as Binhai New Area (see red area in Fig. 9). This was possibly forced by the government policy -"Tianjin City Master Plan (2005–2020)", which for the first time clarified that Tianjin's urban spatial structure evolved from a single core to a dual core, and proposed "the city's industrial layout shifting to the coast".

The urban expansion would lead to decreases of the other land cover types, and this is usually unidirectional, that is, once a land is transformed into urban, it often cannot be converted back [51]. Therefore, we only count the proportion of land occupied by urban expansion in Tianjin from 1985 to 2018 and found

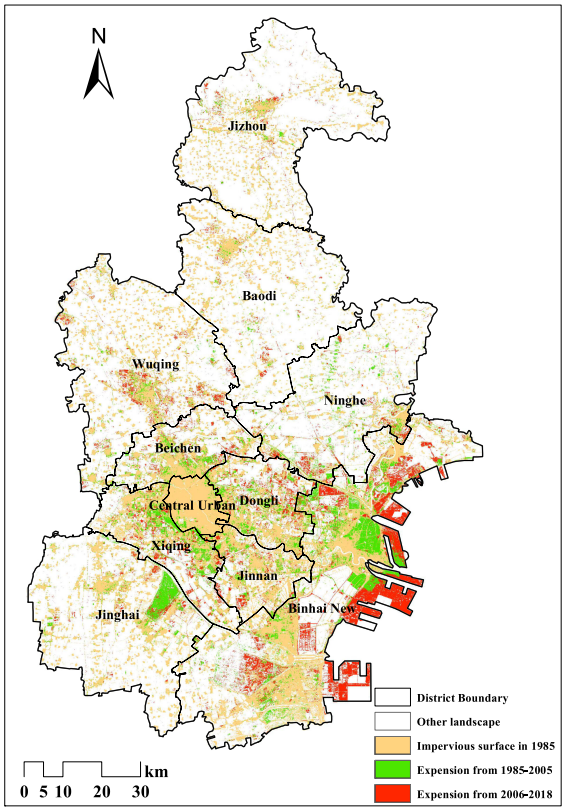

Fig. 9. Impervious surface expansion of Tianjin between 1985 and 2018. Other landscape indicates other all land covers besides of impervious surface.

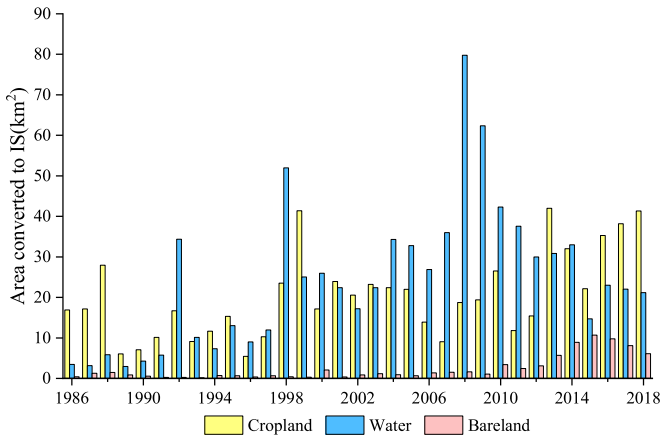

Fig. 10. Illustration of urban expansion from cropland, water, and bareland in Tianjin from 1986 to 2018. IS: impervious surface.

that the urban was transformed mainly from cropland, water, and bareland (Fig. 10). In the first stage (before 2005), the conversions were mainly from cropland and paddy field around the central area. Note that the paddy field is often flooded and will be reasonably classified as water, but we can easily identify them based on some prior knowledge (e.g., they often locate around other croplands). Especially between 1992 and 1998, there are many paddy fields converted into urban. However, the urban area mainly began to expand from water around the coastlines since 2006. In 2008, the water contribution rate reached 79.50% with a total area of 80 km^2, and it was mostly concentrated in the coast of Binhai New Area. In addition, the proportion of bareland encroached in the later period increased slightly, and the conversion area was mainly concentrated in Binhai New Area.

V. Conclusion

We corrected the BRDF effects for LTS and integrated a spatial feature (i.e., line density) into the CCDC algorithm to improve land cover change and classification. The results demonstrated that the combination of BRDF correction and line density can improve the accuracy of land cover change detection and classification significantly. The annual land cover products provide a new insight for understanding the urban expansion process in Tianjin, China.

Acknowledgment

We thank anonymous reviewers for their constructive comments and suggestions. Landsat images were downloaded from the USGS Earth Resources Observation and Science Center (https://espa.cr.usgs.gov). The MATLAB code of CCDC was downloaded from the GitHub page of Global Environmental Remote Sensing Laboratory, the University of Connecticut (https://github.com/gersl/ccdc).

References

[1] C. Sun, Z. F. Wu, Z. Q. Lv, N. Yao, and J. B. Wei, "Quantifying different types of urban growth and the change dynamic in Guangzhou using multi-temporal remote sensing data," *Int. J. Appl. Earth Observ. Geoinformation*, vol. 21, no. 1, pp. 409–417, 2013.

[2] B. Chai and P. Li, "Annual urban expansion extraction and spatio-temporal analysis using Landsat time series data: A case study of Tianjin, China," *IEEE J. Sel. Topics Appl. Earth Observ. Remote Sens.*, vol. 11, no. 8, pp. 2644–2656, Aug. 2018.

[3] M. A. Wulder *et al.*, "Current status of Landsat program, science, and applications," *Remote Sens. Environ.*, vol. 225, pp. 127–147, 2019.

[4] Z. Zhu *et al.*, "Continuous monitoring of land disturbance based on Landsat time series," *Remote Sens. Environ.*, vol. 238, 2020, Art. no. 111116.

[5] C. E. Woodcock *et al.*, "Free access to Landsat imagery," *Science*, vol. 320, no. 5879, pp. 1011–1011, 2008.

[6] Z. Zhu *et al.*, "Benefits of the free and open Landsat data policy," *Remote Sens. Environ.*, vol. 224, pp. 382–385, 2019.

[7] R. E. Kennedy, Z. Yang, and W. B. Cohen, "Detecting trends in forest disturbance and recovery using yearly Landsat time series: 1. LandTrendr — Temporal segmentation algorithms," *Remote Sens. Environ.*, vol. 114, no. 12, pp. 2897–2910, Dec. 2010.

[8] C. Huang, S. N. Goward, J. G. Masek, N. Thomas, Z. Zhu, and J. E. Vogelmann, "An automated approach for reconstructing recent forest disturbance history using dense Landsat time series stacks," *Remote Sens. Environ.*, vol. 114, no. 1, pp. 183–198, Jan. 2010.

[9] E. Hamunyela, J. Verbesselt, and M. Herold, "Using spatial context to improve early detection of deforestation from Landsat time series," *Remote Sens. Environ.*, vol. 172, pp. 126–138, Jan. 2016.

[10] S. Jin, L. Yang, P. Danielson, C. Homer, J. Fry, and G. Xian, "A comprehensive change detection method for updating the National Land Cover Database to circa 2011," *Remote Sens. Environ.*, vol. 132, pp. 159–175, 2013.

[11] J. Verbesselt, A. Zeileis, and M. Herold, "Near real-time disturbance detection using satellite image time series," *Remote Sens. Environ.*, vol. 123, pp. 98–108, Aug. 2012.

[12] J. Verbesselt, R. Hyndman, A. Zeileis, and D. Culvenor, "Phenological change detection while accounting for abrupt and gradual trends in satellite image time series," *Remote Sens. Environ.*, vol. 114, no. 12, pp. 2970–2980, Dec. 2010.

[13] B. DeVries, J. Verbesselt, L. Kooistra, and M. Herold, "Robust monitoring of small-scale forest disturbances in a tropical montane forest using Landsat time series," *Remote Sens. Environ.*, vol. 161, pp. 107–121, May 2015.
[14] L. P. Dutrieux, C. C. Jakovac, S. H. Latifah, and L. Kooistra, "Reconstructing land use history from Landsat time-series: Case study of a swidden agriculture system in Brazil," *Int. J. Appl. Earth Observ. Geoinformation*, vol. 47, pp. 112–124, 2016.
[15] L. Chen, R. Michishita, and B. Xu, "Abrupt spatiotemporal land and water changes and their potential drivers in Poyang Lake, 2000–2012," *ISPRS J. Photogrammetry Remote Sens.*, vol. 98, pp. 85–93, 2014.
[16] Z. Zhu and C. E. Woodcock, "Continuous change detection and classification of land cover using all available Landsat data," *Remote Sens. Environ.*, vol. 144, pp. 152–171, 2014.
[17] Z. Zhu, C. E. Woodcock, C. Holden, and Z. Yang, "Generating synthetic Landsat images based on all available Landsat data: Predicting Landsat surface reflectance at any given time," *Remote Sens. Environ.*, vol. 162, pp. 67–83, 2015.
[18] B. Pengra, A. L. Gallant, Z. Zhu, and D. Dahal, "Evaluation of the initial thematic output from a continuous change-detection algorithm for use in automated operational land-change mapping by the US Geological Survey," *Remote Sens.*, vol. 8, no. 10, 2016, Art. no. 811.
[19] Z. Zhu *et al.*, "Optimizing selection of training and auxiliary data for operational land cover classification for the LCMAP initiative," *ISPRS J. Photogrammetry Remote Sens.*, vol. 122, pp. 206–221, Dec. 2016.
[20] J. F. Brown *et al.*, "Lessons learned implementing an operational continuous United States national land change monitoring capability: The Land change monitoring, assessment, and projection (LCMAP) approach," *Remote Sens. Environ.*, vol. 238, 2020, Art. no. 111356.
[21] P. Fu and Q. Weng, "A time series analysis of urbanization induced land use and land cover change and its impact on land surface temperature with Landsat imagery," *Remote Sens. Environ.*, vol. 175, pp. 205–214, Mar. 2016.
[22] C. Deng and Z. Zhu, "Continuous subpixel monitoring of urban impervious surface using Landsat time series," *Remote Sens. Environ.*, vol. 238, Oct. 2020, Art. no. 110929.
[23] T. M. Berhane *et al.*, "Land-cover changes to surface-water buffers in the midwestern USA: 25 years of Landsat data analyses (1993–2017)," *Remote Sens.*, vol. 12, no. 5, 2020, Art. no. 754.
[24] D. Sulla-Menashe, M. A. Friedl, and C. E. Woodcock, "Sources of bias and variability in long-term Landsat time series over Canadian boreal forests," *Remote Sens. Environ.*, vol. 177, pp. 206–219, 2016.
[25] S. Qiu, Y. Lin, R. Shang, J. Zhang, L. Ma, and Z. Zhu, "Making Landsat time series consistent: Evaluating and improving Landsat analysis ready data," *Remote Sens.*, vol. 11, no. 1, 2019, Art. no. 51.
[26] D. P. Roy, Z. Li, H. K. Zhang, and H. Huang, "A conterminous United States analysis of the impact of Landsat 5 orbit drift on the temporal consistency of Landsat 5 Thematic Mapper data," *Remote Sens. Environ.*, vol. 240, 2020, Art. no. 111701.
[27] D. P. Roy *et al.*, "A general method to normalize Landsat reflectance data to nadir BRDF adjusted reflectance," *Remote Sens. Environ.*, vol. 176, pp. 255–271, 2016.
[28] B. Guindon, Y. Zhang, and C. Dillabaugh, "Landsat urban mapping based on a combined spectral–spatial methodology," *Remote Sens. Environ.*, vol. 92, no. 2, pp. 218–232, 2004.
[29] J. Zhang, P. Li, and J. Wang, "Urban built-up area extraction from Landsat TM/ETM+ images using spectral information and multivariate texture," *Remote Sens.*, vol. 6, no. 8, pp. 7339–7359, 2014.
[30] X. Zhu and D. Liu, "Accurate mapping of forest types using dense seasonal Landsat time-series," *ISPRS J. Photogrammetry Remote Sens.*, vol. 96, pp. 1–11, Oct. 2014.
[31] C. Gómez, J. C. White, and M. A. Wulder, "Optical remotely sensed time series data for land cover classification: A review," *ISPRS J. Photogrammetry Remote Sens.*, vol. 116, pp. 55–72, 2016.
[32] H. Müller, P. Rufin, P. Griffiths, A. J. Barros Siqueira, and P. Hostert, "Mining dense Landsat time series for separating cropland and pasture in a heterogeneous Brazilian savanna landscape," *Remote Sens. Environ.*, vol. 156, pp. 490–499, Jan. 2015.
[33] K. Jia *et al.*, "Land cover classification of finer resolution remote sensing data integrating temporal features from time series coarser resolution data," *ISPRS J. Photogrammetry Remote Sens.*, vol. 93, pp. 49–55, Jul. 2014.
[34] C. L. Arnold and C. J. Gibbons, "Impervious surface coverage: The emergence of a key environmental indicator," *J. Amer. Planning Assoc.*, vol. 62, no. 2, pp. 243–258, Jun. 1996.
[35] G. Meng, The theory and practice of free economic zones: A case study of Tianjin, People's Republic of China, Ph.D. dissertation. Feb. 2003.
[36] Z. Zhu, S. Wang, and C. E. Woodcock, "Improvement and expansion of the Fmask algorithm: Cloud, cloud shadow, and snow detection for Landsats 4–7, 8, and Sentinel 2 images," *Remote Sens. Environ.*, vol. 159, pp. 269–277, Mar. 2015.
[37] P. Gong *et al.*, "Finer resolution observation and monitoring of global land cover: First mapping results with Landsat TM and ETM+ data," *Int. J. Remote Sens.*, vol. 34, no. 7, pp. 2607–2654, Apr. 2013.
[38] M. C. Hansen *et al.*, "High-resolution global maps of 21st-century forest cover change," *Science*, vol. 342, no. 6160, pp. 850–853, 2013.
[39] Z. Zhu and C. E. Woodcock, "Automated cloud, cloud shadow, and snow detection in multitemporal Landsat data: An algorithm designed specifically for monitoring land cover change," *Remote Sens. Environ.*, vol. 152, pp. 217–234, Sep. 2014.
[40] C. B. Schaaf *et al.*, "First operational BRDF, albedo nadir reflectance products from MODIS," *Remote Sens. Environ.*, vol. 83, no. 1, pp. 135–148, Nov. 2002.
[41] M. Claverie *et al.*, "The harmonized Landsat and sentinel-2 surface reflectance data set," *Remote Sens. Environ.*, vol. 219, pp. 145–161, Dec. 2018.
[42] W. Wanner, X. Li, and A. H. Strahler, "On the derivation of kernels for kernel-driven models of bidirectional reflectance," *J. Geophysical Res., Atmos.*, vol. 100, no. D10, pp. 21077–21089, 1995.
[43] C. Deng, C. Li, Z. Zhu, W. Lin, and L. Xi, "Subpixel urban impervious surface mapping: The impact of input Landsat images," *ISPRS J. Photogrammetry Remote Sens.*, vol. 133, pp. 89–103, Nov. 2017.
[44] P. A. Burrough, P. F. M. van Gaans, and R. A. MacMillan, "High-resolution landform classification using fuzzy k-means," *Fuzzy Sets Syst.*, vol. 113, no. 1, pp. 37–52, Jul. 2000.
[45] J. T. Tou and R. C. Gonzalez, "Pattern recognition principles," *Appl. Math. Comput.*, vol. 7, pp. 75–109, 1974.
[46] M. Fauvel, J. Chanussot, J. A. Benediktsson, and J. R. Sveinsson, "Spectral and spatial classification of hyperspectral data using SVMs and morphological profiles," in *Proc. IEEE Int. Geosci. Remote Sens. Symp.*, 2007, pp. 4834–4837.
[47] J. Lee, R. Haralick, and L. Shapiro, "Morphologic edge detection," *IEEE J. Robot. Autom.*, vol. 3, no. 2, pp. 142–156, Apr. 1987.
[48] S. Qiu, Z. Zhu, and B. He, "Fmask 4.0: Improved cloud and cloud shadow detection in Landsats 4–8 and Sentinel-2 imagery," *Remote Sens. Environ.*, vol. 231, Sep. 2019, Art. no. 111205.
[49] P. Gong and P. J. Howarth, "The use of structural information for improving land-cover classification accuracies at the rural-urban fringe," *Photogrammetric Eng. Remote Sens.*, vol. 56, no. 1, pp. 67–73, 1990.
[50] A. H. Fielding and J. F. Bell, "A review of methods for the assessment of prediction errors in conservation presence/absence models," *Environmental Conservation*, vol. 24, no. 1, pp. 38–49, 2002.
[51] A. Schneider, "Monitoring land cover change in urban and peri-urban areas using dense time stacks of Landsat satellite data and a data mining approach," *Remote Sens. Environ.*, vol. 124, pp. 689–704, Sep. 2012.

Yuwei Guan received the B.S. and M.S. degrees in surveying and mapping from the Northeastern University and Technology, Shenyang, China and the University of Electronic Science and Technology of China, Chengdu, China, in 2012 and 2015, respectively.

She is currently an experimentalist with the School of Environment and Resources, University of Electronic Science and Technology of China. Her current research interests include quantitative estimation of land change from satellite remote sensing.

Yanru Zhou is currently working toward the M.S. degree in surveying and mapping from the University of Electronic Science and Technology of China, Chengdu, China.

Her research interests mainly include land change detection and analysis using time series of remote sensing images.

Binbin He received the B.S. degree in resource exploration engineering and the M.S. degree in geology from the Chengdu University of Technology, Chengdu, China, in 1996 and 2002, respectively, and the Ph.D. degree in photogrammetry and remote sensing from China University of Mining and Technology, Xuzhou, China, in 2005.

He is currently a Professor with the School of Environment and Resources, the University of Electronic Science and Technology of China, Chengdu, China. His current research interests include quantitative estimation of land change from satellite remote sensing, and spatiotemporal data mining based on big data.

Xiangzhuo Liu received the B.S. and M.S. degrees in surveying and mapping from the Xi'an University of Science and Technology, Xi'an, China and the University of Electronic Science and Technology of China, Chengdu, China, in 2016 and 2019, respectively. He is currently working toward the Ph.D degree in environment physics from the University of Bordeaux and INRA Center of Bordeaux Aquitaine, Bordeaux, France.

His research interests include wildfire variables extraction from satellite data and vegetation remote sensing.

Hongguo Zhang received the B.S. degree in spatial information and digital technology from the Chengdu University of Technology, Chengdu, China, in 2014. He is currently working toward the Ph.D. degree in remote sensing science and technology from the University of Electronic Science and Technology of China, Chengdu, China.

Shilei Feng received the B.S. degree in geographic information science from the Huazhong Agricultural University, Wuhan, China, in 2017. He is currently working toward the M.S. degree in electronic and communication engineering from the University of Electronic Science and Technology of China, Chengdu, China.

His research interests include cropland mapping and spatio-temporal analysis.